Int J Adv Manuf Technol (2013) 65:717–733
DOI 10.1007/s00170-012-4211-3

ORIGINAL ARTICLE

Modeling of residual stresses in milling

Jiann-Cherng Su · Keith A. Young · Kong Ma · Shesh Srivatsa · John B. Morehouse · Steven Y. Liang

Received: 7 May 2008 / Accepted: 27 April 2012 / Published online: 26 May 2012

Abstract A model to predict residual stresses produced from milling is presented. It uses process conditions as inputs and predicts surface and subsurface residual stress profiles due to milling. The model formulation incorporates cutting force and cutting temperature predictions and utilizes those parameters to define the thermomechanical loading experienced by the workpiece. Model predictions are compared with published experimental data for both cutting forces and residual stress profiles. The results show that the model performs well in predicting residual stress trends for various milling conditions. Residual stress magnitudes as well as profiles are well predicted with the modeling approach.

Keywords Milling forces · Workpiece temperature · Contact stresses · Shear stresses · Hybrid algorithm · Stress relaxation

J.-C. Su
Sandia National Laboratory,
Albuquerque, NM, USA

K. A. Young
The Boeing Company,
Seattle, WA, USA

K. Ma
Rolls Royce Corporation,
Indianapolis, IN, USA

S. Srivatsa
General Electric Aircraft Engines,
Atlanta, GA, USA

J. B. Morehouse · S. Y. Liang (✉)
Georgia Institute of Technology,
Atlanta, GA, USA
e-mail: steven.liang@me.gatech.edu

1 Introduction

Residual stresses play an important role in the performance of machined components. The characteristics that are influenced by residual stress include fatigue life, corrosion resistance, and part distortion. The functional behavior of machined components can be enhanced or impaired by residual stresses. Because of this, understanding the residual stress imparted by machining is an important aspect of understanding machining and overall part quality. Although a tremendous amount of research has been performed on machining-induced residual stress, the majority of it has been focused on orthogonal cutting and turning [1–4].

Milling differs from orthogonal cutting and turning operations in several key areas. In milling, the relative orientation between the cutter tip and the newly generated surface varies during the cut. An additional result of the cutter rotation is the variable depth of cut during chip formation. Furthermore, depending on the geometry of the milling cutter, the surface being generated can be attributed to different parts of the cutter. These factors can affect the residual stresses generated from milling.

Previous research in milling-induced residual stress has been limited to a handful of works. Fuh [5] developed an empirical model to predict the residual stresses produced by milling of 2014-T6 aluminum. The mathematical model incorporated cutting conditions such as cutting speed, feed, and cutting depth as well as tool geometry characteristics such as nose radius and flank wear. The research utilized a response surface methodology coupled with a Takushi method to limit the number of required experiments. The mathematical model implemented second-order polynomial to produce a relationship between the residual stress and cutting

parameters. The curve fitting technique provided little insight into the physical relationship between the cutting parameters and the residual stress. Jacobus [6] showed the significance of location on residual stresses due to milling AISI 4340. Mantle [7] experimented on surface integrity generated from milling gamma titanium aluminide.

Based on the review of literature relating to milling-induced residual stress, opportunities for advancing modeling capabilities still exist. The current understanding of residual stresses generated from milling is limited empirical modeling and experimental results. The goal of this research is to provide an analytical model for predicting residual stresses due to milling based on cutting parameters, cutting conditions, and workpiece material properties. The modeling approach is completely predictive in the sense that it takes the process inputs and material parameters and produces force predictions, workpiece temperature predictions, and residual stress profiles generated by machining. The model provides an advantage over previous efforts because it does not require extensive calibration in order to function. It also produces results quickly, thus potentially enabling its use as an optimization tool. The modeling results are compared with experimental data for validation.

2 Modeling

Te research seeks to achieve the objectives offered previously through analytical modeling of the cutting process. To that aim, the process will be modeled from a physics-based approach with a focus on cutting force, workpiece temperature, and contact stress modeling. A flowchart of the methodology is shown in Fig. 1.

As the figure shows, the model takes cutting process conditions such as speed, feed, and depth of cut along with tool geometry and material properties and inputs them into models for predicting cutting forces and cutting temperatures. The cutting forces are predicted from the process parameters. The results are fed into the thermal models to predict the temperature rise in the workpiece due to machining. The outputs from these modeling areas are then used to predict the thermomechanical loading experienced by the workpiece and, subsequently, the residual stress formed.

2.1 Milling force modeling

The milling force model used in this research is based on the force modeling introduced by Li [8]. The modeling approach discretizes the milling cutter into axial segments as shown in Fig. 2. The cutting action of each slice is treated as an oblique cut, with each edge having an inclination angle equal to the helix angle β of the cutter [8]. The corner radius r_{corner} presents additional challenges with respect to cutting force predictions. In order to utilize the orthogonal/oblique force models, the effect of the corner radius being engaged during the cut must also be modeled. The use of an equivalent straight cutting edge C_S^* to capture the effect on the corner radius has been used by previous researchers [9–11].

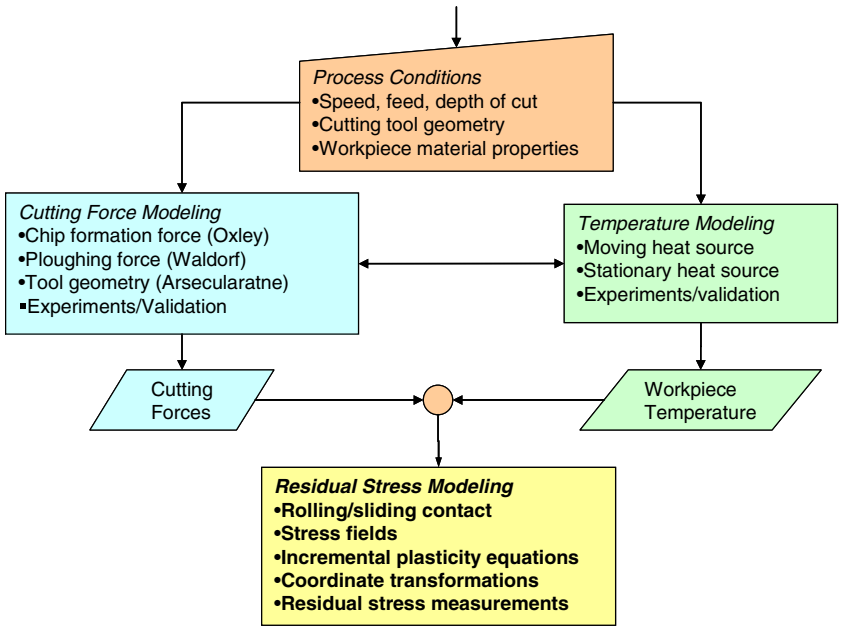

Fig. 1 Residual stress model flowchart

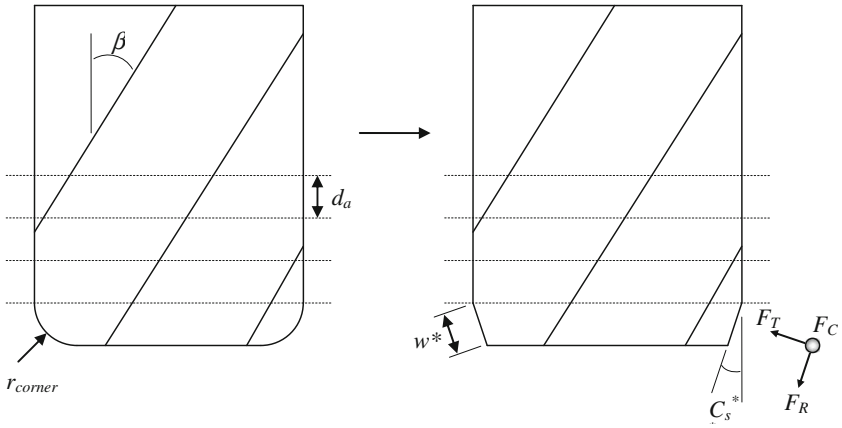

Fig. 2 Axial slicing of helical end mill

In orthogonal cutting, two force components exist. The force in the direction of the cut is called the cutting force F_C and the force normal to the newly generated surface is called the thrust force F_T. For oblique cutting, an additional force component F_R exists due to the inclination angle i (Fig. 3). In order to predict F_R, the inclination angle, chip flow angle η_c, and rake angle α_n need to be known. From Stabler's flow rule [12], the chip flow angle is equal to the inclination angle as shown in Eq. (1).

$$\eta_c = i \tag{1}$$

If F_C and F_T are known, then the expression for the resultant force F_R is given by Eq. (2):

$$F_R = \frac{F_C(\sin i - \cos i \sin \alpha_n \tan \eta_c) - F_T \cos \alpha_n \tan \eta_c}{\sin i \sin \alpha_n \tan \eta_c + \cos i}. \tag{2}$$

The equivalent cutting conditions are used to predict the cutting forces F_C, F_T, and F_R. Those forces are then transformed to represent forces in the cutting, feed, and radial directions P_1, P_2, and P_3, respectively, shown in Fig. 4. The transformation is given by Eq. (3).

$$\begin{aligned} P_1 &= F_C \\ P_2 &= -F_T \cos\left(C_S^*\right) - F_R \sin\left(C_S^*\right) \\ P_3 &= F_T \sin\left(C_S^*\right) - F_R \cos\left(C_S^*\right) \end{aligned} \tag{3}$$

After the forces are predicted for each slice, an additional transformation is performed to represent the cutting forces in the workpiece coordinate system. The force contribution from each slice is then summed to produce the total milling force as a function of the cutter rotational position. The total forces (Eq. (4)) from the combination of elemental slices correspond to the forces measured by the dynamometer.

$$\begin{aligned} F_X(\phi) &= \sum_{j=1}^{r} \sum_{k=1}^{N_t} P_{1j,k} \cos\left(\phi_{j,k}\right) - P_{2j,k} \sin\left(\phi_{j,k}\right) \\ F_Y(\phi) &= \sum_{j=1}^{r} \sum_{k=1}^{N_t} P_{1j,k} \sin\left(\phi_{j,k}\right) + P_{2j,k} \cos\left(\phi_{j,k}\right) \\ F_Z(\phi) &= \sum_{j=1}^{r} \sum_{k=1}^{N_t} P_{3j,k} \end{aligned} \tag{4}$$

In the Eq. (4), r is the number of axial slices in the cutter and N_t is the number of flutes. The immersion angle $\phi_{j,k}$ of each tooth depends on the helix angle β and the height of the slice along the axis of the cutter. The expression for the immersion angle for each slice of each tooth is given by Eq. (5).

$$\phi_{j,k} = \phi - (k-1)\phi_{\text{pitch}} - \frac{2\tan(\beta)}{D} z(j) \tag{5}$$

In the above equation, ϕ is the rotational position of the cutter, D is the diameter of the cutter, and $z(j)$ is the height of the cutter slice in the axial direction. ϕ_{pitch} is the cutter pitch given by Eq. (6).

$$\phi_{\text{pitch}} = \frac{2\pi}{N_t} \tag{6}$$

If the axial depth of cut is larger than the corner radius, the first slice of the cutter is considered to include the entire corner radius. The rest of the cutter that is engaged in cutting is divided into axial steps. The number of axial steps chosen depends on the cutting conditions. Because milling is an intermittent cutting process, one additional aspect of modeling milling forces is establishing whether or not the flute is engaged in cutting. In up milling, the maximum chip thickness occurs at the end of the cut. For down milling, the maximum chip thickness occurs at the beginning of the cut. The angular region in which the cutter is engaged in cutting is known as the immersion angle [13]. A summary of the entry and exit angles for the various milling operations is provided in Table 1.

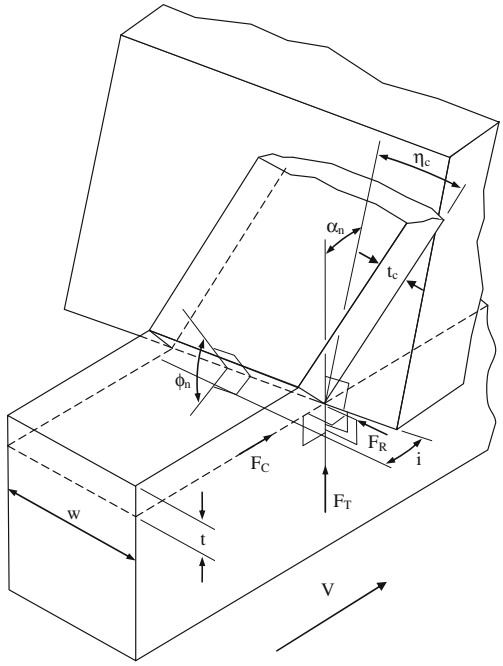

Fig. 3 Oblique chip formation model [14]

Each oblique cutting edge is assumed to consist of two sources of forces: chip formation and plowing forces. The chip formation cutting force model chosen for this work is based on Oxley's predictive machining theory [14]. It is a slip-line cutting force model derived from experimental observations in metal cutting. Plane strain, steady-state conditions are assumed. The outputs for the model include the shear angle ϕ, flow stress in the shear zone, cutting force F_C, and thrust force F_T.

The force contribution due to the roundness of the cutting edge is also considered. The model developed by Waldorf [15] is used in the present study to predict the plowing forces due to tool edge roundness. It is a slip-line model developed for predicting plowing forces in orthogonal cutting that incorporates a small, stable built-up edge of material adhering to the cutting tool.

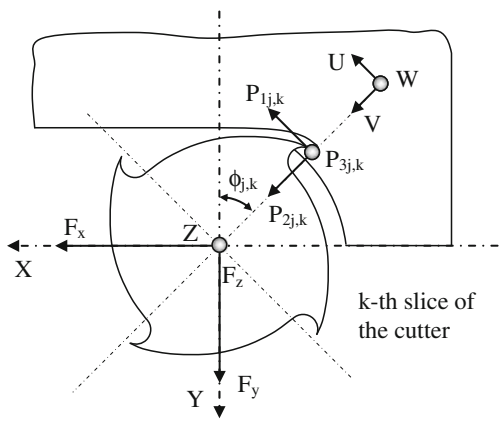

Fig. 4 Coordinate system for slice of milling cutter [8]

Table 1 Summary of entry and exit angles for milling operations

Milling type	Entry angle	Exit angle
Up milling	0°	$\arccos\left(\frac{D-2d_r}{D}\right)$
Down milling	$-\arccos\left(\frac{D-2d_r}{D}\right)$	0°
Slot milling	0°	180°

In Fig. 5, r_e is the edge radius, α is the rake angle, ϕ is the shear angle, and t_c is the uncut chip thickness. The fan field angles θ, γ, and η are found from geometric and friction relationships. Details for computing those values are available in [15]. R is the radius of the circular fan field centered at A. If the flow stress k of the material is known along with the shear angle ϕ, the plowing forces can determined from Eq. (7). P_{cut} is the plowing force in the cutting direction, P_{thrust} is the plowing force normal to the newly generated surface, and w is the width of cut.

$$P_{cut} = k \cdot w \begin{bmatrix} \cos(2\eta)\cos(\phi-\gamma+\eta)+ \\ (1+2\theta+2\gamma+\sin(2\eta))\sin(\phi-\gamma+\eta) \end{bmatrix} \cdot \mathrm{CA}$$
$$P_{thrust} = k \cdot w \begin{bmatrix} (1+2\theta+2\gamma+\sin(2\eta))\cos(\phi-\gamma+\eta)- \\ \cos(2\eta)\sin(\phi-\gamma+\eta) \end{bmatrix} \cdot \mathrm{CA} \quad (7)$$

where $\mathrm{CA}=R/\sin\eta$.

The total cutting forces for each flute are the sum of the chip formation forces and the plowing forces. As a result, the total force in the cutting direction and the thrust direction are given by Eq. (8).

$$\begin{aligned} F_{cut\_total} &= F_C + P_{cut} \\ F_{thrust\_total} &= F_T + P_{thrust} \end{aligned} \quad (8)$$

2.2 Workpiece temperature modeling

The thermal effects due to the cutting process can have a significant effect on the residual stresses produced.

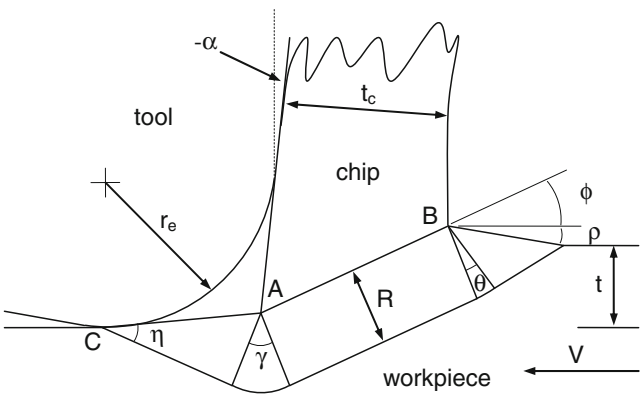

Fig. 5 Waldorf's slip-line field for plowing [15]

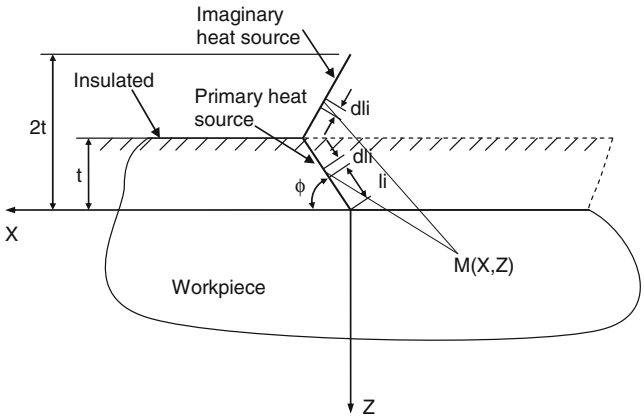

Fig. 6 Heat transfer model of primary source relative to workpiece [29]

Researchers have shown that increased cutting temperatures result in greater tensile residual stress on the surface of a machined component [1, 16]. Jaeger [17] advanced a method of determining the temperature rise due to moving heat sources. Extensions of his method have been used extensively in the literature to determine the temperature rise due to cutting [18–20]. That same approach to modeling the temperature rise due to cutting will be used in this research.

In modeling the workpiece temperatures, two heat sources are assumed to exist. The first is the primary heat source generated from the shear zone. The second heat source is a result of rubbing between the tool and the workpiece. The workpiece surface is considered to be insulated in this study as illustrated in Fig. 6. To satisfy the adiabatic condition at the workpiece boundary, an imaginary heat source is used [18].

The temperature rise at a point $M(X, Z)$ is the combination of the primary and imaginary heat sources. The total temperature rise at any point $M(X, Z)$ due to the oblique-moving heat source and the imaginary heat source is given by:

$$\theta_{\text{workpiece-shear}}(X,Z) = \frac{q_{\text{shear}}}{2\pi k_{\text{workpiece}}} \int_0^L e^{-\frac{(X-l_i\sin\phi)V_{\text{cut}}}{2a_{\text{workpiece}}}} \left\{ K_0\left[\frac{V_{\text{cut}}}{2a_{\text{workpiece}}}\sqrt{(X-l_i\sin\varphi)^2+(Z-l_i\cos\varphi)^2}\right] + K_0\left[\frac{V_{\text{cut}}}{2a_{\text{workpiece}}}\sqrt{(X-l_i\sin\varphi)^2+(Z+l_i\cos\varphi)^2}\right]\right\} dl_i \tag{9}$$

where $\varphi = \left(\phi - \frac{\pi}{2}\right)$ and $L = \frac{t}{\sin\phi}$.

A similar application of the moving heat source is used to determine the temperature rise due to rubbing between the tool edge and the workpiece. The temperature rise in the workpiece due to rubbing is given by Eq. (10) (Fig. 7).

$$\theta_{\text{workpiece-rubbing}}(X,Z) = \frac{1}{\pi k_{\text{workpiece}}} \int_0^{VB} \gamma \cdot q_{\text{rubbing}}(x) e^{-\frac{(X-x)V_{\text{cut}}}{2a_{\text{workpiece}}}} K_0\left[\frac{V_{\text{cut}}}{2a_{\text{workpiece}}}\sqrt{(X-x)^2+(Z)^2}\right] dx \tag{10}$$

γ in the Eq. (10) is a partition of heat transferred into the workpiece during cutting. An approximate value for the partition ratio based on material properties of the tool and the workpiece is given by Eq. (11), where k, ρ, C, k_t, ρ_t, and C_t are the thermal conductivity, density, and specific heat of the workpiece and tool, respectively [21].

$$\gamma = \frac{\sqrt{k\rho C}}{\sqrt{k\rho C} + \sqrt{k_t\rho_t C_t}}, \tag{11}$$

The heat sources q_{shear} and q_{rubbing} are determined from the cutting parameters and the cutting force models described in the previous section. The resulting expressions for the shear plane heat source and the rubbing heat source are given by Eqs. (12) and (13), respectively.

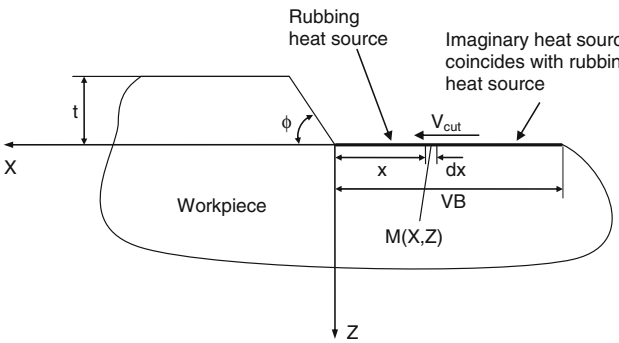

Fig. 7 Heat transfer model of rubbing heat source relative to workpiece [29]

$$q_{\text{shear}} = \frac{(F_c \cos\phi - F_t \sin\phi)(V_{\text{cut}} \cos\alpha / \cos(\phi - \alpha))}{(t)(w)\csc\phi} \tag{12}$$

$$q_{\text{rubbing}} = \frac{P_{\text{cut}} V_{\text{cut}}}{(w)VB} \tag{13}$$

For machining with coolant, the cooling effect is treated as a stationary heat sink. The coolant is assumed to be applied behind the tool as shown in Fig. 8. By treating the coolant as a stationary heat sink, the analytical model for predicting the temperature rise due to a stationary heat source can be used [22].

The temperature drop in the workpiece due to the stationary heat source associated with the coolant is given by the equation:

$$\theta_{\text{cool}}(X,Z) = \frac{q_{\text{cool}}}{2\pi k_t} \int_0^l \int_{-w/2}^{w/2} \left(\frac{1}{R_i} + \frac{1}{R_i'}\right) dy dx \tag{14}$$

In Eq. (14), l is the distance behind the tool tip to which coolant is acting, w is the width of the cut region, $R_i = \sqrt{(X_2 - x_i)^2 + (Y_2 - y_i)^2 + Z_2^2}$ and $R_i' = \sqrt{(X_2 - (2L_{\text{VB}} - x_i))^2 + (Y_2 - y_i)^2 + Z_2^2}$. The heat loss intensity q_{cool} is given by Eq. (15), where $\overline{h}$ is the overall heat transfer coefficient, T is the temperature rise of the workpiece due to the shear plane and rubbing heat sources, and T_0 is the ambient temperature.

$$q_{\text{cool}} = \overline{h}(T - T_0) \tag{15}$$

The net change in the temperature of the workpiece due to machining and coolant is the superposition of the two heat sources and one heat sink.

$$\theta_{\text{total}}(X,Z) = \theta_{\text{shear}}(X,Z) + \theta_{\text{rub}}(X,Z) + \theta_{\text{cool}}(X,Z) \tag{16}$$

2.3 Residual stress modeling

In order to model residual stresses, the stress history experienced by the machined part needs to be known. A rolling/sliding contact approach is used in the present work to capture the stress history. This type of model assumes that every location at a specified depth in the workpiece that passes beneath the moving load experiences the same thermomechanical load history. The passing load produced by rolling contact is similar to that generated in the cutting process.

Two sources of mechanical stress due to cutting are considered. One is due to contact between the tool edge and the workpiece, and the other is from the stresses in the shear zone. The tool edge contributes to a normal load coupled with a tangential load. The shear zone adds an inclined shear stress and normal stress. These two sources comprise the stress history experienced by the workpiece. Both are illustrated in Fig. 9. Assuming the stress profiles in these regions are known, the stresses in the workpiece are computed by integrating the solutions for normal and tangential point loads over the region of contact as shown in Eq. (17).

$$\begin{aligned}
\sigma_x &= -\tfrac{2z}{\pi} \int_{-b}^{a} \tfrac{p(s)(x-s)^2}{\left[(x-s)^2+z^2\right]^2} ds - \tfrac{2}{\pi} \int_{-b}^{a} \tfrac{q(s)(x-s)^3}{\left[(x-s)^2+z^2\right]^2} ds \\
\sigma_z &= -\tfrac{2z^3}{\pi} \int_{-b}^{a} \tfrac{p(s)}{\left[(x-s)^2+z^2\right]^2} ds - \tfrac{2z^2}{\pi} \int_{-b}^{a} \tfrac{q(s)(x-s)}{\left[(x-s)^2+z^2\right]^2} ds \\
\tau_{xz} &= -\tfrac{2z^2}{\pi} \int_{-b}^{a} \tfrac{p(s)(x-s)}{\left[(x-s)^2+z^2\right]^2} ds - \tfrac{2z}{\pi} \int_{-b}^{a} \tfrac{q(s)(x-s)^2}{\left[(x-s)^2+z^2\right]^2} ds
\end{aligned} \tag{17}$$

The normal pressure in the contact region due to the tool tip is assumed to be two-dimensional Hertzian. The magnitude of the stress is determined from the geometry of the contact region. An analytical solution to Eq. (17) exists for Hertzian contact [10]. The solution requires the maximum

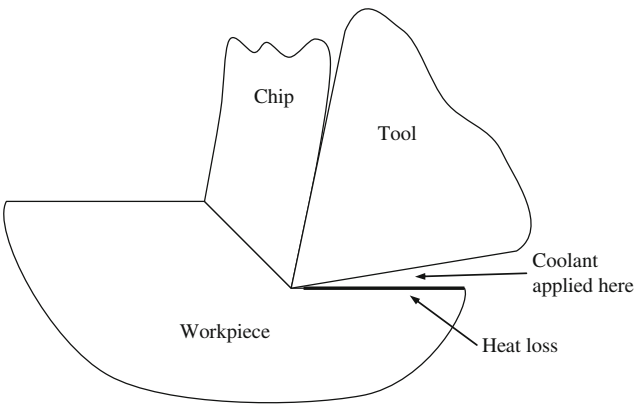

Fig. 8 Schematic of heat loss source due to coolant

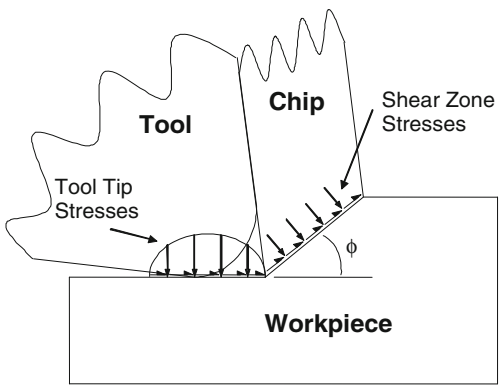

Fig. 9 Stress sources in residual stress formation

Hertzian pressure p_0 due to the normal load shown in Eq. (18), where a is approximated as one half CA from Waldorf's plowing force model. The shear stress at the surface τ is assumed to be uniformly distributed and proportional to the stress induced by the plowing cutting force P_{cut} and the coefficient of friction μ. It is also shown in Eq. (19).

$$p_0 = \frac{2P_{\text{thrust}}}{\pi(wa)} \tag{18}$$

$$\tau = \mu\left(\frac{P_{\text{cut}}}{w \cdot \text{CA}}\right) \tag{19}$$

In addition to the stresses induced by the edge hone, the stresses in the shear plane are treated as a constant value equal to the flow stress of the material in that region. This type of approach has been used in previous research [16, 23]. A plot of the stress contours in the workpiece due to the combined loads is shown in Fig. 10.

Using the stress fields captured from the forces, contact zones, and thermal predictions, the residual stresses are computed from a rolling/sliding contact algorithm developed by McDowell [24]. The algorithm captures desirable aspects of previous rolling/sliding contact models [25, 26]. The model provides a robust, stable prediction of subsurface plasticity and residual stresses over a wide range of loading conditions. Because of this, it is well suited for the type of contact experienced by the workpiece during the cutting process. It also admits arbitrary forms of kinematic hardening for nonproportional cyclic plasticity. The loading determines the subsurface residual stress and the size of the subsurface plastic zone.

The hybrid algorithm uses a blending function Ψ which is dependent on the instantaneous value of the modulus ratio h/G. G is the elastic shear modulus, h is the modulus function, and κ is an algorithm constant. The blending function is shown in Eq. (20).

$$\Psi = 1 - \exp\left(-\kappa\frac{3}{2}\frac{h}{G}\right), \tag{20}$$

In the hybrid algorithm, neither the assumption of 0 strain rate in the cutting direction $\dot{\varepsilon}_{xx} = 0$ [25] nor the assumption of elastic stress in the cutting direction $\dot{\sigma}_{xx} = \dot{\sigma}_{xx}{}^*$ [26] is assumed during plastic flow. For elastic–plastic loading, the blending function is used to describe the strain rate in the rolling/cutting direction as shown in Eq. (21). Similarly, for the plane strain condition transverse to the rolling/cutting direction, the strain rate expression is given by Eq. (22). Both equations are modified from the original expressions in [24] to account for thermal strain in the present application.

$$\begin{aligned}\dot{\varepsilon}_{xx} &= \tfrac{1}{E}\left[\dot{\sigma}_{xx} - \nu\left(\dot{\sigma}_{yy} + \dot{\sigma}_{zz}{}^*\right)\right] + \alpha\Delta T + \tfrac{1}{h}\left(\dot{\sigma}_{xx}n_{xx} + \dot{\sigma}_{yy}n_{yy} + \dot{\sigma}_{zz}{}^*n_{zz} + 2\,\dot{\tau}_{xz}{}^*n_{xz}\right)n_{xx} \\ &= \Psi\left(\tfrac{1}{E}\left[\dot{\sigma}_{xx}{}^* - \nu\left(\dot{\sigma}_{yy} + \dot{\sigma}_{zz}{}^*\right)\right] + \alpha\Delta T + \tfrac{1}{h}\left(\dot{\sigma}_{xx}{}^*n_{xx} + \dot{\sigma}_{yy}n_{yy} + \dot{\sigma}_{zz}{}^*n_{zz} + 2\,\dot{\tau}_{xz}{}^*n_{xz}\right)n_{xx}\right)\end{aligned} \tag{21}$$

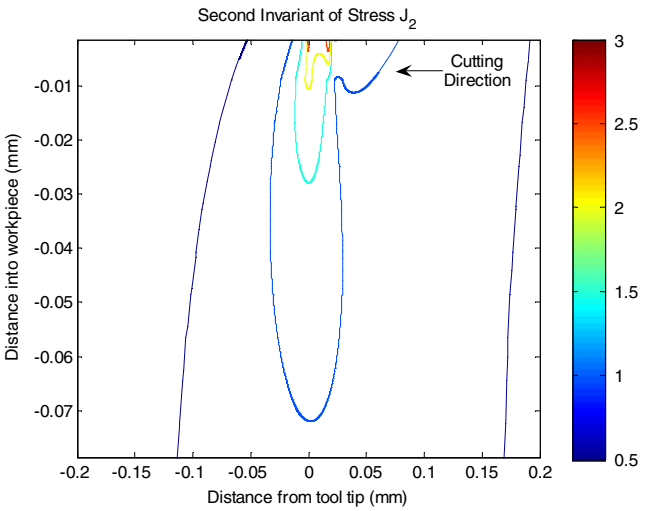

Fig. 10 Stress field contours in workpiece

Table 2 Equations used in incremental plasticity

Equation Description	Equation
von Mises yield surface	$F = \frac{3}{2}(S_{ij} - \alpha_{ij})(S_{ij} - \alpha_{ij}) - k^2 = 0$
Deviatoric stress	$S_{ij} = \sigma_{ij} - (\sigma_{kk}/3)\delta_{ij}$
Plastic strain rate (normality flow rule)	$\dot{\varepsilon}_{ij}p = \frac{1}{h}\left\langle \dot{S}_{kl}n_{kl}\right\rangle n_{ij}$
Components of unit normal in plastic strain	$n_{ij} = \frac{S_{ij}-\alpha_{ij}}{\sqrt{2}k}$
Rate direction (on yield surface)	
Evolution of back stress for linear kinematic hardening	$\dot{\alpha}_{ij} = \left\langle \dot{S}_{kl}n_{kl}\right\rangle n_{ij}$

Table 3 Milling experimental conditions

Case	Speed (rpm)	Type	Tool	Number of flutes	Chip load (mm/flute)	Axial DOC (mm)	Radial DOC (mm)	D (mm)	r (mm)
1	344	Down	W-C	4	0.080	8.89	0.89	19.05	3.05
2	344	Slot	W-C	4	0.080	0.89	–	19.05	3.05
3	509	Slot	W-C	6	0.080	0.25	–	25.40	3.05
4	509	Slot	W-C	6	0.080	2.03	–	25.40	3.05
5	1,528	Down	W-C	10	0.080	20.32	0.89	25.40	3.05
6	1,146	Down	W-C	10	0.080	0.76	17.78	25.40	3.05
7	191	Down	HSS	4	0.080	20.32	0.89	19.05	3.05
8	191	Down	HSS	4	0.080	0.760	17.78	19.05	3.05

$$\dot{\varepsilon}_{yy} = \frac{1}{E}\left[\dot{\sigma}_{yy} - \nu\left(\dot{\sigma}_{xx} + \dot{\sigma}^{*}_{zz}\right)\right] + \alpha\Delta T + \frac{1}{h}\left(\dot{\sigma}_{xx}n_{xx} + \dot{\sigma}_{yy}n_{yy} + \dot{\sigma}^{*}_{zz}n_{zz} + 2\,\dot{\tau}^{*}_{xz}n_{xz}\right)n_{yy} = 0 \tag{22}$$

The above equations are solved simultaneously to determine the increments in stress for $\dot{\sigma}_{xx}$ and $\dot{\sigma}_{yy}$. The expressions are integrated over the passage of the load to determine the residual stresses due to cutting. Additional equations necessary for implementing the incremental plasticity model are shown in Table 2.

In the model, residual stresses and strains should satisfy the boundary conditions described by Merwin and Johnson [27] shown in Eq. (23).

$$\begin{array}{llll} (\varepsilon_x)_r = 0 & (\sigma_x)_r = f_1(z) & (\varepsilon_y)_r = 0 & (\sigma_y)_r = f_2(z) \\ (\varepsilon_z)_r = f_3(z) & (\sigma_z)_r = 0 & (\gamma_{xz})_r = f_4(z) & (\tau_{xz})_r = 0 \end{array} \tag{23}$$

Meeting these boundary conditions after the passage of the load is necessary because during the loading cycle, equilibrium conditions do not exist. The nonzero components σ^R_{zz}, τ^R_{xz}, ε^R_{xx}, and T^R are incrementally relaxed until the boundary conditions are met. If M steps are used for the relaxation process, then the stress increments are

$$\Delta\sigma_{zz} = -\frac{\sigma^R_{zz}}{M}, \quad \Delta\tau_{xz} = -\frac{\tau^R_{xz}}{M}, \quad \Delta\varepsilon_{xx} = -\frac{\varepsilon^R_{xx}}{M}, \text{ and } \quad \Delta T = -\frac{T^R}{M}. \tag{24}$$

During relaxation, there are two possibilities: purely elastic relaxation and elastic–plastic relaxation. For purely elastic relaxation, $F<0$ or $F=0$ and $dS_{ij}n_{ij}\geq 0$. The increments for σ_{xx} and σ_{yy} are given by Eq. (25). For elastic–plastic relaxation, Eqs. (21) and (22) are solved for $\Delta\sigma_{xx}$ and $\Delta\sigma_{yy}$, where $\Delta's$ replace the time derivatives. At the end of the relaxation procedure, both σ_{xx} and σ_{yy} will be nonzero. The results are the true residual stresses that remain in the body.

$$\begin{aligned} \Delta\sigma_{xx} &= \frac{E\Delta\varepsilon_{xx} + (1+\nu)(\Delta\sigma_{zz}\nu - E\alpha\Delta T)}{(1-\nu^2)} \\ \Delta\sigma_{yy} &= \frac{\nu E\Delta\varepsilon_{xx} + (1+\nu)(\Delta\sigma_{zz}\nu - E\alpha\Delta T)}{(1-\nu^2)} \end{aligned} \tag{25}$$

3 Experimental details

The experimental data for milling were collected as part of the Metals Affordability Initiative (MAI) Machining Distortion program [28]. Cutting forces were measured using a Kistler Milling Dynamometer while milling Ti 6Al-4V. Measurements of tool deflection and dimensional control

Table 4 X-ray diffraction measurement conditions

Parameter	Value	Parameter	Value
Target	0.154 nm	Psi tilts	10
Target power	200 W (30kv,6.7 mA)	Tilts	(0, 20.00, 14.03, 7.42, 0.66)
Material	Ti 6Al-4V	Collection time	2 s×20 exposures
X-ray elastic constant	84.116 GPa	Total collection time	5 min
Crystallographic plane	{213}	Psi zero assignment	Curve fit elliptical
Bragg angle	142°		

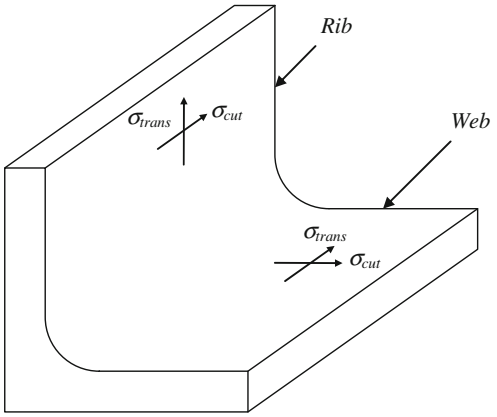

Fig. 11 Orientation of stress measurements for milling samples

were also performed. Specimens were generated in order to measure machining-induced residual stress for typical machining parameters. Care was taken to ensure that cutting force frequencies were low enough to be captured by the dynamometer. Consequently, force measurements were taken at lower spindle rotational speeds. These speeds were still within standard machining practices (0.25 to 0.51 surface m/s). Castrol 6519 ClearEdge lubricant was used during the machining. It is a water-based, water-soluble cutting fluid. It was applied in a flood manner through 6.4-mm diameter nozzles at low pressure.

The experimental test conditions are shown in Table 3. In Table 3, D is the cutter diameter and r is the corner radius of the cutter. For each of the conditions, the edge sharpness is assumed to be 7.0 μm. Tungsten carbide and high-speed steel cutters are used. Cases 1–4 are used to validate the cutting force model for milling. Residual stresses are measured for cases 5–8.

Electro-polishing and X-ray diffraction measurements were performed on the four specimens at a technical service provider (Proto Manufacturing). Measurements were made at 0.005-mm intervals up to 0.051 mm into the workpiece.

Table 5 Relative average milling forces for cases 1–4

Case	Force direction	Average predicted	Average measured	% Error
1	Fx	1.10	1.00	9.6
	Fy	1.40	1.31	6.7
	Fz	0.02	0.13	80.9
2	Fx	0.66	1.00	34.3
	Fy	3.15	2.59	21.8
	Fz	2.51	1.76	42.3
3	Fx	0.76	1.00	23.7
	Fy	2.73	3.10	12.2
	Fz	2.10	1.99	5.9
4	Fx	1.69	1.00	68.7
	Fy	4.30	2.73	57.4
	Fz	1.01	0.71	41.9

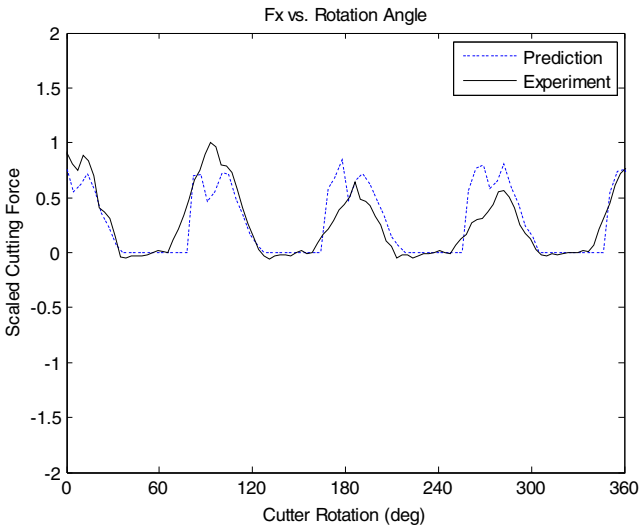

Fig. 12 Milling force Fx results for case 1

Beyond 0.051 mm, measurements were made at 0.013-mm intervals until 0.127 mm. X-ray measurements in the remainder of the material were taken at 0.025-mm intervals. The conditions used for the measurements are shown in Table 4.

The specimens were generated with the side and the end of the milling cutters. For all machining tests, end mills were new with sharp cutting edges. The surface generated with the side of the end mill is referred to as the rib, and the surface generated with the corner radius is the called the web. Both of these regions are illustrated in Fig. 11.

4 Results and discussion

The results for the force predictions are shown below. Fx, Fy, and Fz represent forces in the feed, normal to the feed, and axial directions, respectively. Each of the plots captures

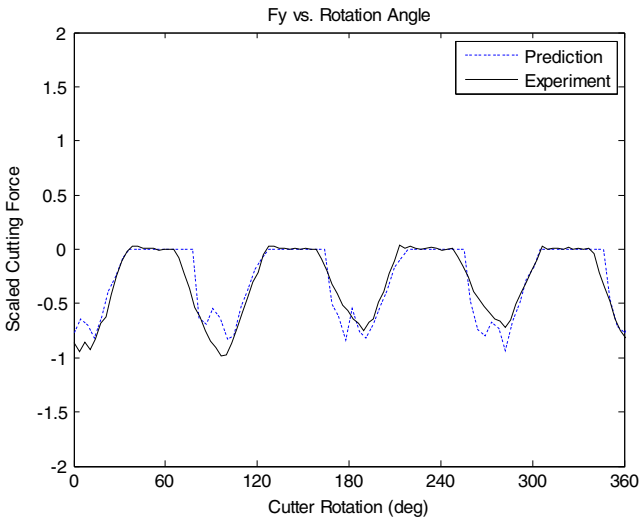

Fig. 13 Milling force Fy results for Case 1

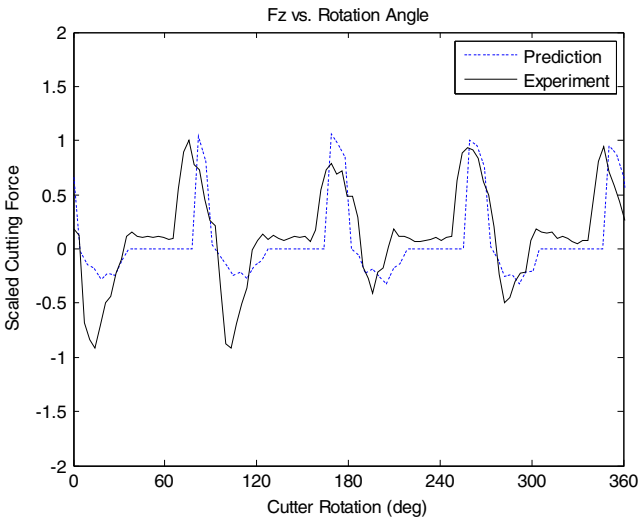

Fig. 14 Milling force Fz results for case 1

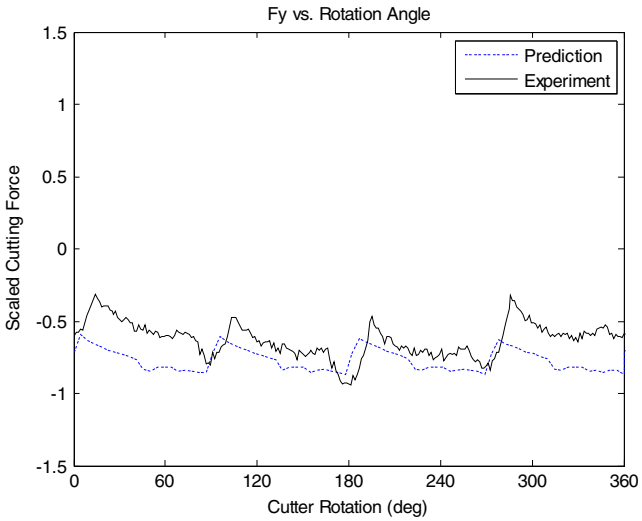

Fig. 16 Milling force Fy results for case 2

the cutting forces for one revolution of the milling cutter. The average cutting forces for each revolution are shown in Table 5. All force predictions are made assuming the coefficient of friction due to the lubrication is μ=0.4 and the overall heat transfer coefficient $\overline{h} = 2,000 \frac{W}{m^2 - °C}$. The cutting force data are presented relative to the maximum measured value of force for each cutting direction.

The cutting force predictions for case 1 match the experimental data very well in terms of force magnitudes and shape. The conditions for case 1 are representative of those used in finishing cuts and rib cuts. The cutting conditions are such that the axial depth of cut is greater than the corner radius. Therefore, both the rounded portion of the cutter and straight segment of the cutter are engaged. Cutting on the corner radius causes a positive axial force. Cutting that occurs on the straight edge of the cutter causes a negative axial force due to the helix angle. The balance of forces in the axial direction changes from positive to negative throughout the rotation of the cutter. These effects are captured in Figs. 12, 13 and 14. The milling force model also captures the duration of engagement of each cutting tooth.

Case 2 is a slot milling operation with a moderate axial depth of cut. Only a portion of the corner radius is engaged for the cutting condition. As a result, the axial force is completely positive. Similar to case 1, the engagement and disengagement of the flutes during the cutter rotation are captured very well by the predictive model. Forces in the feed direction Fx are shown in Fig. 15. The relative predicted forces oscillate from around −0.5 to 0.0 as the flutes engage and disengage. The relative average force per revolution is approximately −0.3. The measured forces oscillate from −1.0 to 0.2 with an average value of approximately −0.4. The results are similar for forces in the direction normal to feed Fy. The predicted forces oscillate between approximately −0.6

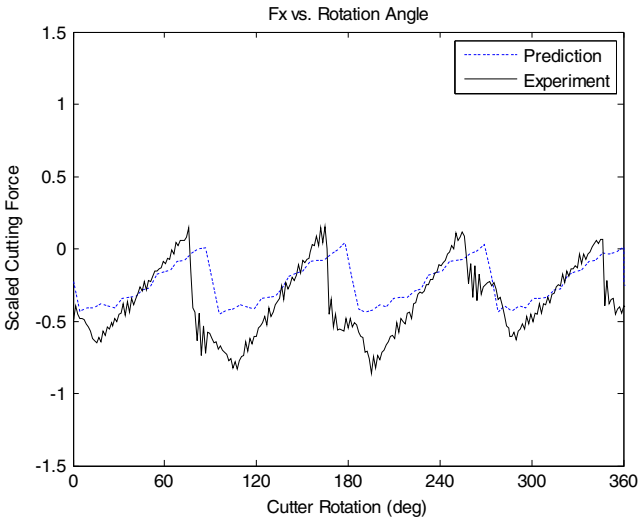

Fig. 15 Milling force Fx results for case 2

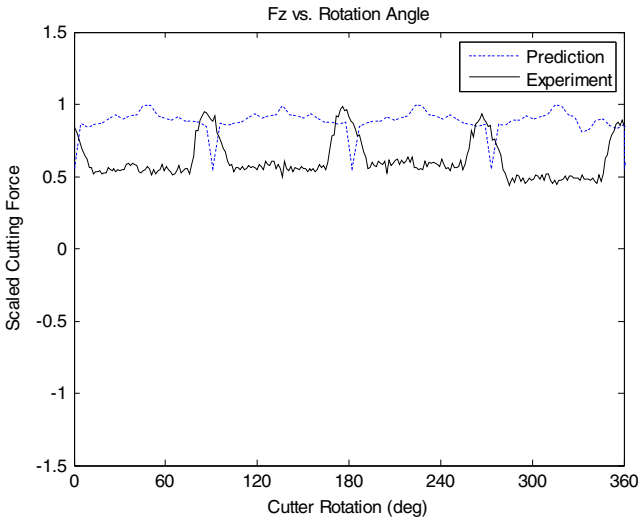

Fig. 17 Milling force Fz results for case 2

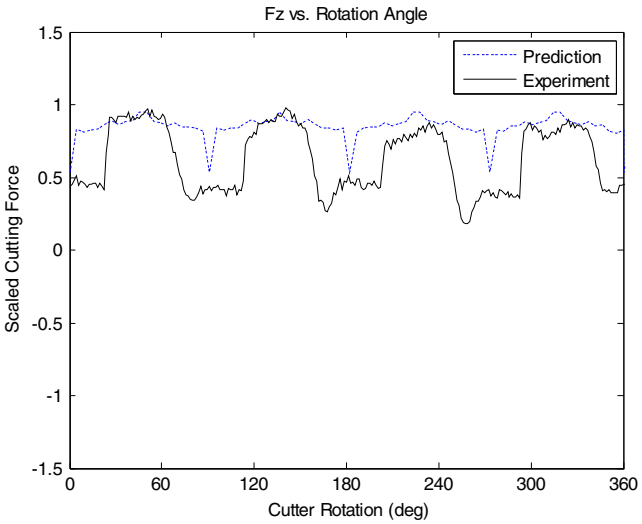

Fig. 18 Additional milling force Fz results for case 2

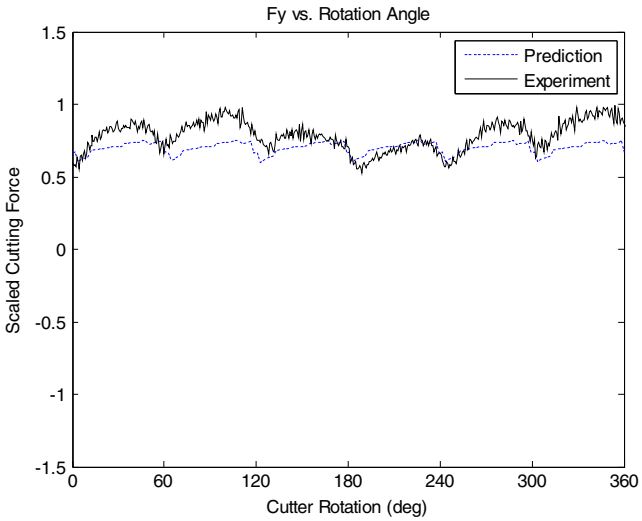

Fig. 20 Milling force Fy results for case 3

and −0.9 with the average force over the rotation −0.8. The measured forces range from −0.4 to -1.0 and have an average force of -0.7.

In both cases, the shape of the force profile during the cutter revolution is captured well by the predictive model even though the cutting force magnitudes differ from the experimental data. The discrepancy can be attributed in part to cutter runout. The runout can be seen in Figs. 15 and 16 as variations in the force peaks during the cutter rotation.

Radial runout is due to the axis of rotation of the spindle and axis of rotation of the cutter being out of alignment. Because the magnitude of the runout is comparable to the chip load during milling, it can be a source of considerable variation in cutting forces. In spite of the runout, the milling force model performs well at predicting forces in the feed and normal directions.

While the forces predicted in the feed and normal direction are very good for case 2, there is a noticeable difference between predicted cutting forces and measured cutting forces is in the axial direction as shown in Fig. 17. The experimental data show force peaks at approximately 90°, 180°, 270°, and 360°. However, the predictions show dips in the cutting forces at those positions. This discrepancy is of note due to the fact that for other slot milling conditions, the cutting forces at similar positions show force valleys.

For a four-flute cutter in a slot milling operation, two flutes are engaged with the workpiece for a majority of the rotation. However, there is a point in the rotation where theoretically only one flute is engaged. That point in the rotation occurs when the flute engaged in cutting is at 90°. Since the axial forces from each of the flutes act in the same direction, it would be expected that the minimum cutting force occurs when only one flute is cutting. This scenario is

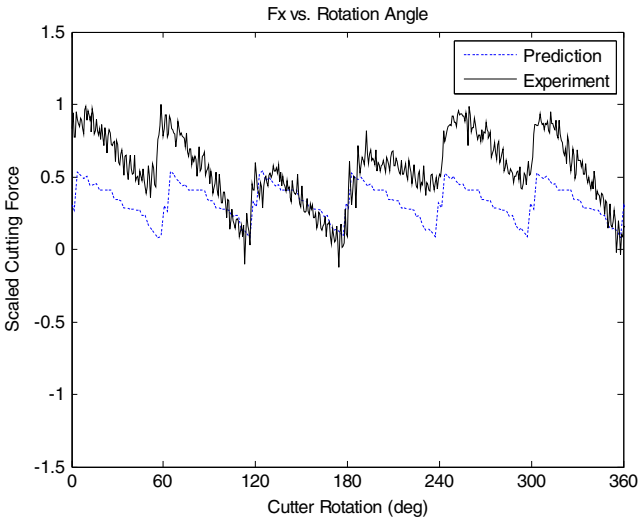

Fig. 19 Milling force Fx results for case 3

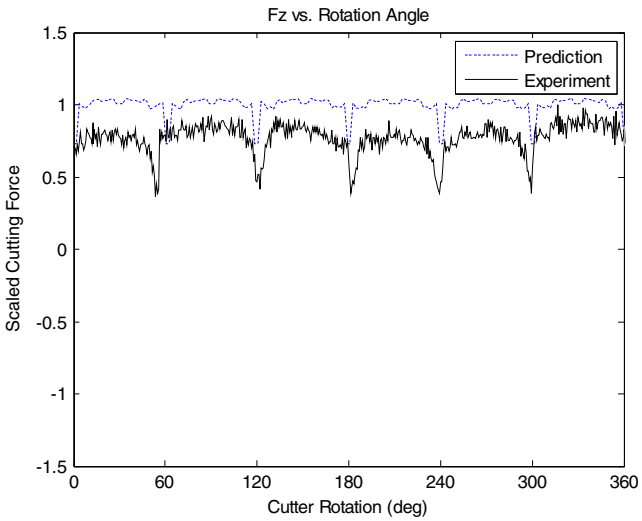

Fig. 21 Milling force Fz results for case 3

captured in the predictive cutting model where the minimum force values are at 90°, 180°, 270°, and 360°. However, in the experimental data, force valleys are found at those locations.

A second set of axial force measurements for the same conditions is utilized in an effort to understand the axial force results. The force data are plotted in Fig. 18. It shows a broader peak for the measured axial forces, closer to what is expected for the cutting conditions. However, the force valley is not as sharp as predicted. The difference between the two data sets shows that variability in measured cutting forces can be significant within the same set of cutting conditions.

Case 3 is also a slot milling operation utilizing a six-flute cutter. The axial depth of cut, like case 2, is smaller than the corner radius. As a result, all of the cutting occurs on the corner radius. The force components in all three directions are well predicted. The shape of the predicted force profiles coincides almost exactly with the measured force profiles as shown in Figs. 19, 20 and 21.

The experimental data show low-frequency force oscillations throughout the cutter rotation. For instance, in Fig. 19, the relative peak cutting feed cutting force at 60° is approximately 1.0. However, at 120°, the cutting force is slightly less than 0.7. For an ideal milling operation, the peak cutting forces at those locations should be the same. The variation in forces, similar to the previous case, indicates the presence of cutter runout. Even with the presence of runout, the model does a very good job of capturing the cutting forces as a function of cutter rotation.

The results for case 4 are shown in Figs. 22, 23 and 24 . The conditions are similar to case 3, except for a larger axial depth of cut. The larger axial depth of cut results in larger cutting forces in all directions. This trend is captured by the predictive model. Similar to case 3, the presence of runout is visible in the experimental data. It induces a low-frequency oscillation in the force data.

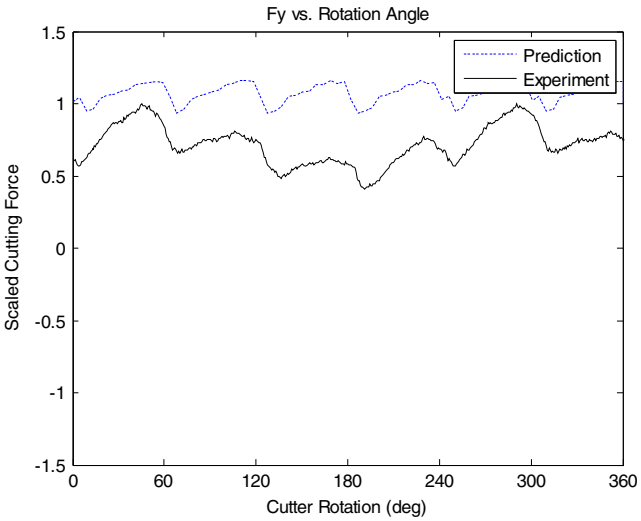

Fig. 23 Milling force Fy results for case 4

The difference between predicted and experimental forces can be attributed to the runout as well as the larger engagement of the corner radius during cutting. The side cutting angle $C_S{}^*$ discussed in the milling force model may be over-predicted for the larger axial depth of cut used in case 4. As a result, the predicted forces will be larger than expected, particularly in the axial direction.

Table 5 summarizes the average cutting force results in cases 1–4. The relative magnitudes of the average milling forces for a single rotation of the cutter are listed. For cases 1–3, the majority of the average cutting forces are within 35 % of the measured average values. The two forces that stand out, however, are the average axial force Fz in cases 1 and 2. Referring to Fig. 14, the regions where the cutter is not engaged with the workpiece should produce zero cutting

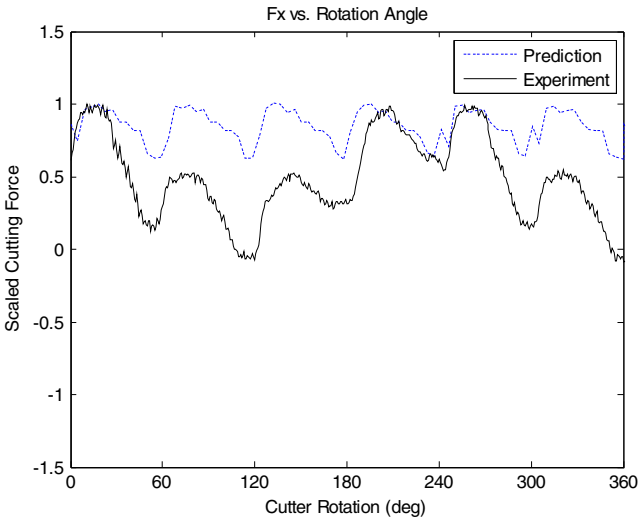

Fig. 22 Milling force Fx results for case 4

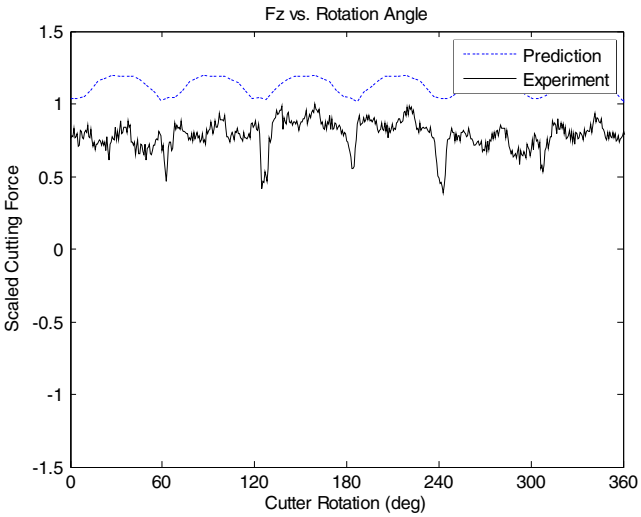

Fig. 24 Milling force Fz results for case 4

force. However, there is an approximately 0.1 relative force offset in the measured axial force. Consequently, the measured average force differs from the predicted average force by what appears to be a significant amount. However, if the 0.1 offset is removed, the computed average for the axial force becomes 0.03. The resulting error is 12 %.

The larger prediction for the average axial force in case 2 is due to the shape of the predicted cutting force. The predictions show a narrow force valley, while the measurement shows a wide force valley. The wider force valley causes the measured average axial force to be lower for a rotation of the cutter.

Average forces for case 4, as Figs. 22, 23 and 24 show, are higher than the measured average forces. This is due in part to the over-prediction of equivalent side cutting angle $C_S{}^*$. The larger axial depth of cut conditions used for case 4 results in greater cutting forces in all directions.

4.1 Milling temperature modeling

The effect of the lubrication is a reduction in the workpiece temperature. Figure 25 provides a typical temperature profile under the tool tip without coolant, while Fig. 26 shows the temperature contour with coolant. The temperature difference at the surface for the cooled condition is approximately 130°C.

Figure 27 compares the temperature difference between dry machining and with the coolant. As would be expected, the greatest temperature difference occurs at the surface. This is due to the greater temperature difference between the workpiece and the coolant at that location and the higher heat loss intensity.

An interesting feature of Fig. 27 is the high temperature gradient. The predicted temperature drops by nearly 350°C within 0.08 mm. This would indicate that the effects of temperature on residual stress are more prominent near the workpiece surface. If residual stresses exist beyond that depth, they will be due to mechanical loading.

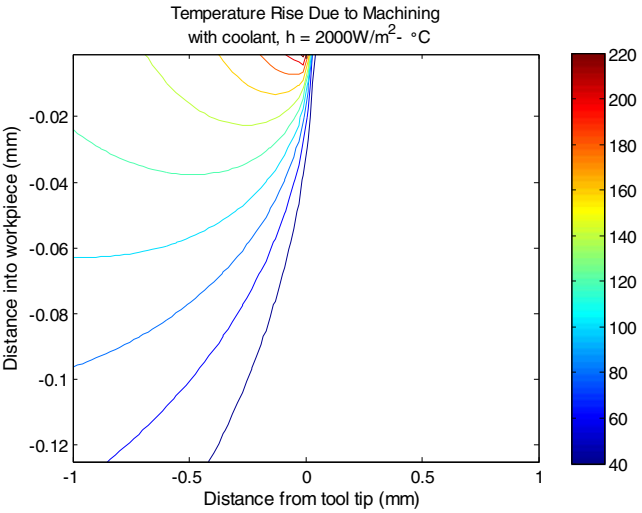

Fig. 26 Temperature contours with coolant

4.2 Milling residual stress results

Residual stress measurements are made on the ribs for cases 5 and 7 and measurements are made on the webs for cases 6 and 8. Force measurements are unavailable for the machining conditions used to generate the samples in cases 5–8. The results from the residual stress measurements and the model predictions are shown below. The residual data are scaled relative to the maximum measured value in the cut direction for case 5. The residual stresses were measured to a depth of 0.381 mm, although the values oscillated about 0 beyond approximately 0.076 mm. Because of this, the residual stresses are treated as diminishing to 0 beyond

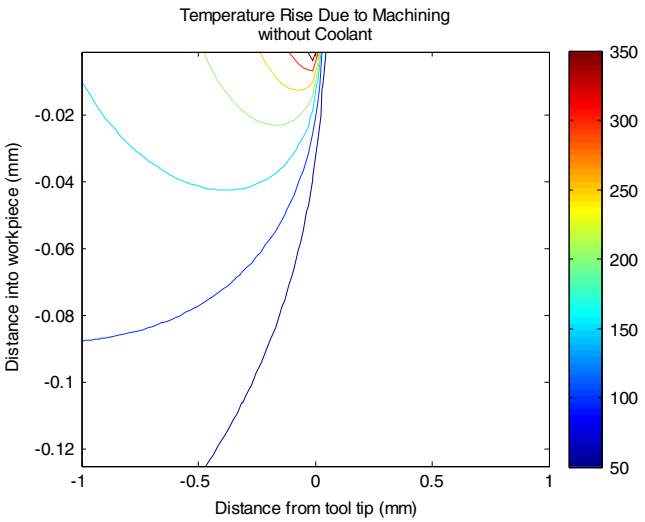

Fig. 25 Temperature contours without coolant

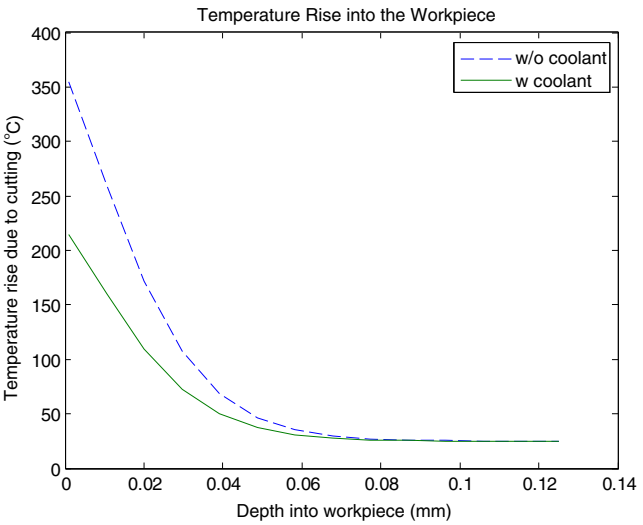

Fig. 27 Temperature rise directly beneath the tool tip

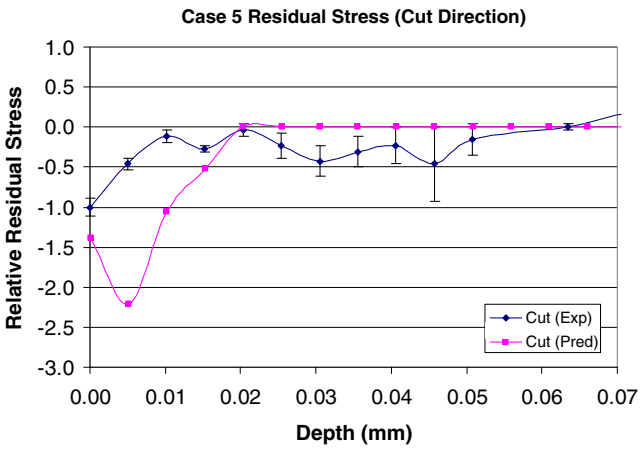

Fig. 28 Residual stress results in cut direction for case 5

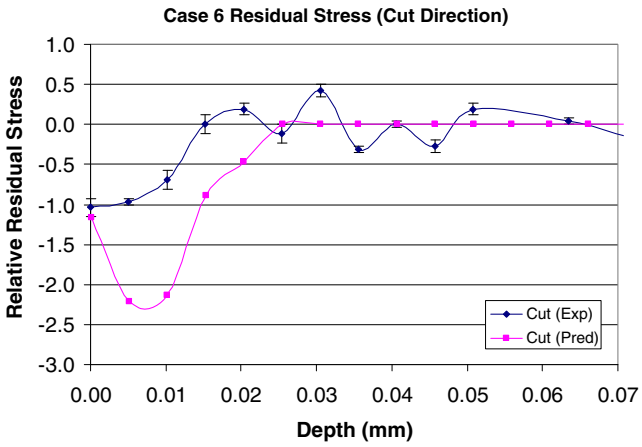

Fig. 30 Residual stress results in cut direction for case 6

0.076 mm. The data plotted below show the residual stresses between the surface and 0.076 mm below the surface. Error bars for each of the measured data points indicate the standard deviation for the data point. The standard deviation information was provided by Proto as part of the measurement data.

The residual stress results for case 5 are shown in Figs. 28 and 29. The data show low levels of compressive residual stress produced by the cutting process. The maximum compressive residual stress exists at the surface and has a relative value of approximately −1.0 in the cut direction and −0.8 in the transverse direction. The penetration of the residual stress produced from cutting is fairly shallow. Due to the oscillation, the exact depth of penetration is difficult to discern. However, judging by the overall trend, the residual stress due to machining appears negligible beyond 0.020 mm.

The predicted residual stresses are of greater magnitude than the measured residual stresses. One significant potential source of that error is the helical geometry of the milling cutter. Due to the helix angle of the cutter, the depth of cut at each rotational position of the cutter varies along the axis of the cutter. As a result, the cutting force varies along the axis of the cutter. Isolating the exact point of cut during the rotation in which the surface of the residual stress measurement is made is not a straight-forward proposition. In the current modeling procedure, the axial slice chosen to represent the cutting forces imparted on the newly generated surface is the one that has the largest depth of cut at the newly formed surface. This assumption could lead to an overestimating of the forces at the surface. However, each of the predictions for the residual stresses in the ribs is made in the same fashion to maintain consistency.

The results for case 6 are shown in Figs. 30 and 31. The residual stresses for case 6 are measured on the web of the machined part. Similar to case 5, the depth of penetration of the residual stresses is reasonably well predicted. Residual stresses in the cut direction diminish to 0, at approximately 0.015 mm. The same is true for the residual stress in the transverse direction. The predicted residual stresses penetrate to approximately 0.025 mm. The residual stresses reach 0, around 0.018 mm. The predictions of residual stresses diminish at approximately 0.025 mm. In both directions, the

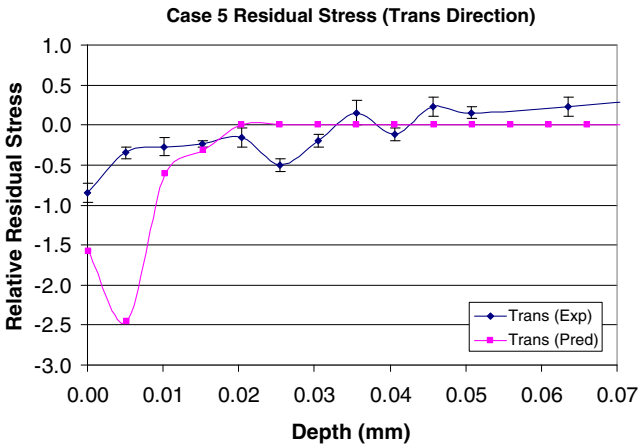

Fig. 29 Residual stress results in transverse direction for case 5

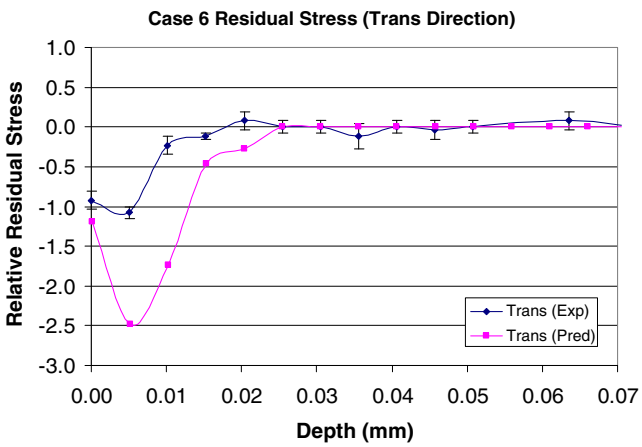

Fig. 31 Residual stress results in transverse direction for case 6

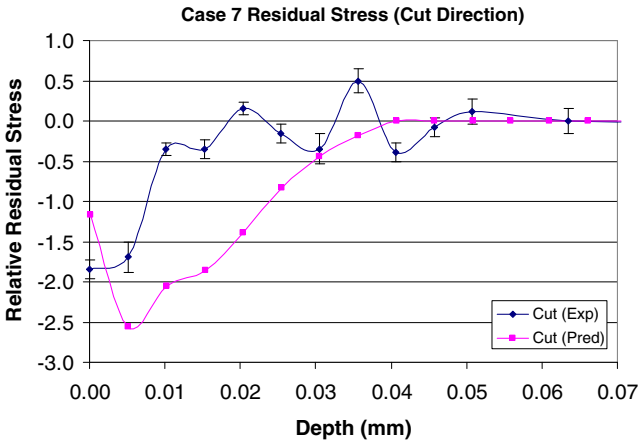

Fig. 32 Residual stress results in cut direction for case 7

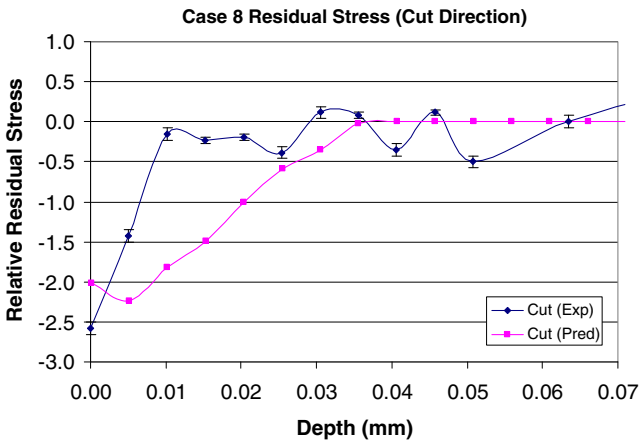

Fig. 34 Residual stress results in cut direction for case 8

residual stresses are slightly over-predicted with regards to magnitudes. The explanation provided for the low compressive residual stresses in case 5 is also relevant to case 6.

Case 7 uses cutting conditions similar to those used in case 5 except for the type of cutter and the cutting speed. The results are shown in Figs. 32 and 33. The conditions used in case 7 yield larger measured compressive residual stresses. For lower cutting speeds, the mechanical loads dominate the residual stress formation. When mechanical loads dominate, the residual stress formation is more compressive [2]. An additional characteristic of the residual stress results for case 7 is the slightly larger depth of penetration.

Both of these traits can be explained from a modeling perspective. The larger depth of penetration of the residual stress is due to its dependence on mechanical loading. For case 7, the predicted shear angle for the slice treated as producing the residual stress is approximately 20°. For case 5, the shear angle is approximately 30°. The lower shear angle produces a larger mechanically stressed zone beneath the newly generated surface. Consequently, the residual stress formation in that region will be more compressive and penetrate deeper beneath the surface.

The residual stress results for case 8 are shown in Figs. 34 and 35. Case 8, like case 6, is a slot milling operation with the measured surface of interest being the web. A large radial depth of cut coupled with a shallow axial depth of cut results in a machined surface that is generated largely by the corner radius. The slow cutting speed results in the mechanical load exerting more dominance compared to the thermal load. Similar to the previous cases, the exact depth of penetration is difficult to isolate from the experimental data. However, the trend with regards to both the compressive nature of the residual stress as well as the depth to which it penetrates is captured by the predictive model.

The comparisons between predicted residual stresses and measured residual stresses show that the predictive model performs well in terms of capturing the depth of penetration as well as the general residual stress profile for milling. In most cases, the predicted residual stress magnitudes are larger than the measured values. This discrepancy can be attributed to the variability in the precise location of the

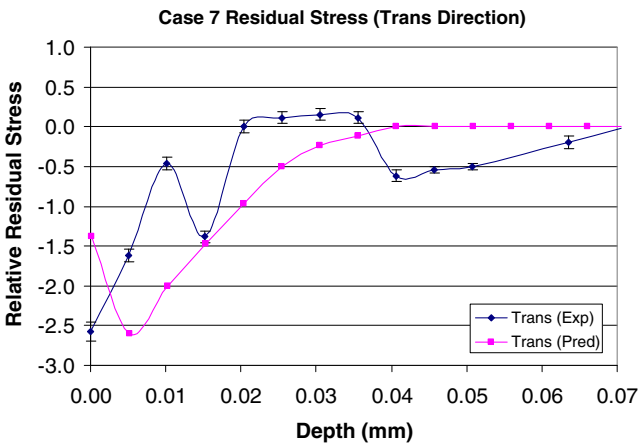

Fig. 33 Residual stress results in transverse direction for Case 7

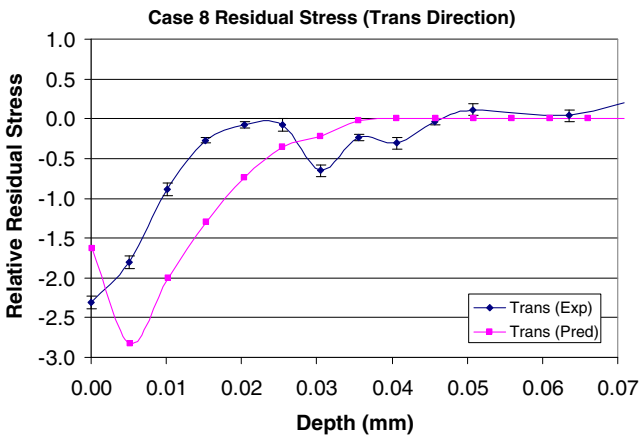

Fig. 35 Residual stress results in transverse direction for case 8

cutting edge that generates the newly formed surface. In spite of this, the model consistently predicts the correct trends for the residual profiles for milling conditions.

5 Conclusions

This research presented a model for predicting residual stress generated from milling operations. The model incorporates cutting force and thermal models derived for orthogonal/oblique cutting conditions considering geometric transformations as well as location effects. Additionally, the effect of cutting fluid is incorporated into the model. Milling experiments are performed on Ti 6Al-4V to measure cutting forces as well as residual stresses produced from milling. Both slot milling and face milling are considered in the modeling predictions.

The milling force predictions show good agreement with the experimental data. The predicted force profiles match the experimental data in terms of force magnitudes and profiles. It is found that the corner radius and the modeling of the corner radius play an important role in force predicted for the axial direction. For depths of cut smaller than the corner radius, there is a pronounced effect on the force predictions.

Residual stresses are measured for four experimental cases. Two measurements are taken on the rib of the machined samples, and two are taken on the web of the machined samples. The residual stress results for cases 5 and 6 showed low levels of compressive residual stress generated from the cutting operation. Cases 7 and 8 produced larger magnitudes of compressive residual stress due in part to slower cutting speeds. The model predictions capture the residual stress trends well. The depth of penetration of residual stress and the compressive nature of the residual stress are captured. However, predictions for the residual stress magnitudes tend to be larger than those measured.

The effects of coolant were introduced into the model. Geometric transformations were made in order to apply the orthogonal model to the more complex milling scenarios. Residual stress measurements were made for several milling conditions. The measured subsurface residual stress profiles were found to be compressive for the cases explored. The model predictions captured the trends of residual stresses produced from the experiments.

Acknowledgments The authors would like to thank the MAI Machining Distortion program for financial support and experimental data. Thanks to Keith Young at Boeing for providing the milling experimental data, Kong Ma at Rolls Royce, and Shesh Shrivatsa at GE for discussions and feedback. Their inputs were greatly appreciated.

References

1. Henriksen EK (1951) Residual stresses in machined surfaces. Am Soc Mech Eng Trans 73(1):69–76
2. Liu CR, Barash MM (1982) Variables governing patterns of mechanical residual stress in a machined surface. J Eng Ind Trans ASME 104(3):257–264
3. Jang DY et al (1996) Surface residual stresses in machined austenitic stainless steel. Wear 194(1–2):168–173
4. Matsumoto Y, Hashimoto F, Lahoti G (1999) Surface integrity generated by precision hard turning. CIRP Ann Manuf Technol 48(1):59–62
5. Fuh K-H, Wu C-F (1995) Residual-stress model for the milling of aluminum alloy (2014-T6). J Mater Process Technol 51(1–4):87–105
6. Jacobus JK, Kapoor SG, DeVor RE (2001) Experimentation on the residual stresses generated by endmilling. J Manuf Sci Eng 123:748–756
7. Mantle AL, Aspinwall DK (2001) Surface integrity of a high speed milled gamma titanium aluminide. Elsevier Science Ltd., Amsterdam
8. Li HZ, Zhang WB, Li XP (2001) Modelling of cutting forces in helical end milling using a predictive machining theory. Int J Mech Sci 43(8):1711–1730
9. Young HT, Mathew P, Oxley PLB (1987) Allowing for nose radius effects in predicting the chip flow direction and cutting forces in bar turning. Proc Inst Mech Eng C Mech Eng Sci 201(3):213–226
10. Young H-T et al (1993) Predicting the chip flow for nose radius tools under oblique machining conditions. J Chin Inst Eng Trans Chin Inst Eng Ser A/Chung-kuo Kung Ch'eng Hsuch K'an 16(6):825–834
11. Arsecularatne JA, Mathew P, Oxley PLB (1995) Prediction of chip flow direction and cutting forces in oblique machining with nose radius tools. Proc Inst Mech Eng B J Eng Manuf 209(B4):305–315
12. Stabler GV (1951) Fundamental geometry of cutting tools. Inst Mech Eng Proc 165(63):14–21
13. Altintas Y (2000) Manufacturing automation: metal cutting mechanics, machine tool vibrations, and CNC design, vol xii. Cambridge University Press, New York, p 286
14. Oxley PLB (1989) The mechanics of machining: an analytical approach to assessing machinability (Ellis Horwood series in mechanical engineering). Halsted, New York, p 242
15. Waldorf DJ, DeVor RE, Kapoor SG (1998) Slip-line field for ploughing during orthogonal cutting. J Manuf Sci Eng Trans ASME 120(4):693–698
16. Lin Z-C, Lin Y-Y, Liu CR (1991) Effect of thermal load and mechanical load on the residual stress of a machined workpiece. Int J Mech Sci 33(4):263–278
17. Jaeger JC (1942) Moving sources of heat and temperature at sliding contacts. R Soc NSW J Proc 76(Part 3):203–224
18. Komanduri R, Hou ZB (2000) Thermal modeling of the metal cutting process part I—temperature rise distribution due to shear plane heat source. Int J Mech Sci 42(9):1715–1752
19. Komanduri R, Hou ZB (2001) Analysis of heat partition and temperature distribution in sliding systems. Wear 251(1–12):925–938
20. Trigger KJ, Chao BT (1951) Analytical evaluation of metal-cutting temperatures. Am Soc Mech Eng Trans 73(1):57–60
21. Sekhon GS, Chenot JL (1993) Numerical simulation of continuous chip formation during non-steady orthogonal cutting. Eng Comput (Swansea, Wales) 10(1):31–48
22. Komanduri R, Hou ZB (2001) Thermal modeling of the metal cutting process—part Ii: temperature rise distribution due to frictional heat source at the tool-chip interface. Int J Mech Sci 43(1):57–88
23. Wu DW, Matsumoto Y (1990) Effect of hardness on residual stresses in orthogonal machining of AISI 4340 steel. J Eng Ind Trans ASME 112(3):245–252

24. McDowell DL (1997) Approximate algorithm for elastic–plastic two-dimensional rolling/sliding contact. Wear 211(2):237–246
25. McDowell DL, Moyar GJ (1986) A more realistic model of non-linear material response: application to elastic–plastic rolling contact. In Proceedings of the 2nd International Symposium on Contact Mechancis and Wear of Rail/Wheel Systems. Kingston, RI
26. Jiang Y, Sehitoglu H (1994) Analytical approach to elastic–plastic stress analysis of rolling contact. J Tribol Trans ASME 116(3):577–587
27. Merwin JE, Johnson KL (1963) An analysis of plastic deformation in rolling contact. Proceedings, Institution of Mechanical Engineers, London 177(25):676–685
28. Metals Affordability Initiative (MAI) Machining Distortion (2006)
29. Huang Y (2002) Predictive modeling of tool wear rate with application to CBN hard turning. Ph.D. thesis, Georgia Institute of Technology, Atlanta, GA